1   Thalamic bursts modulate cortical synchrony locally to switch between states of global functional

2   connectivity in a cognitive task

3

4

5

6

7

8

9   *Oscar Portoles[1,2], Manuel Blesa[3], Marieke van Vugt[1], Ming Cao[2], Jelmer P. Borst[1]

10

[1] Bernoulli Institute for Mathematics, Computer Science and Artificial Intelligence, Faculty of Science and Engineering, University of Groningen, Groningen, 9747 AG, The Netherlands

[2] Engineering and Technology Institute Groningen, Faculty of Science and Engineering, University of Groningen, Groningen, 9747 AG, The Netherlands

[3] MRC Centre for Reproductive Health, University of Edinburgh, Edinburgh EH16 4TJ, UK

Corresponding Author:

*Oscar Portoles:

o.portoles.marin@rug.nl; +31 503635256; Nijenborgh, 9, 9747 AG, Groningen, The Netherlands

11

12   **This PDF file includes:**

13   abstract,
14   author summary,
15   introduction,
16   results (with figures),
17   discussion,
18   methods,
19   acknowledgments,
20   author contributions,
21   declaration of interests,
22   supplemental information,
23   references

1   1

Abstract

24

25 Performing a cognitive task requires going through a sequence of functionally diverse

26 stages. Although it is typically assumed that these stages are characterized by distinct

27 states of cortical synchrony that are triggered by sub-cortical events, little reported

28 evidence supports this hypothesis. To test this hypothesis, we first identified cognitive

29 stages in single-trial MEG data of an associative recognition task, showing with a novel

30 method that each stage begins with local modulations of synchrony followed by a state of

31 directed functional connectivity. Second, we developed the first whole-brain model that can

32 simulate cortical synchrony throughout a task. The model suggests that the observed

33 synchrony is caused by thalamocortical bursts at the onset of each stage, targeted at

34 cortical synapses and interacting with the structural anatomical connectivity. These

35 findings confirm that cognitive stages are defined by distinct states of cortical synchrony

36 and explains the network-level mechanisms necessary for reaching stage-dependent

37 synchrony states.

38

Author summary

40 A novel machine-learning method was applied to unveil the dynamics of local and cortex-wide

41 neural coordination underlying the fundamental cognitive processes involved in a memory task. To

42 explain how neural activity – and ultimately behavior – was coordinated throughout the task, we

43 developed a whole-brain model that incorporates cognitive mechanisms, anatomy, and neural

44 biophysics. Similar models are used with resting state data, however, simulating a cognitive task

45 remained elusive. The model showed that sub-cortical pulses at the onset of cognitive processes – as

46 hypothesized by cognitive and neurophysiological theories – were sufficient to switch between the

47 states of neural coordination observed. These findings have implications to understand goal-directed

48 cognitive processing and the mechanisms to reach states of neural coordination.

2   2

49

50 **Key words**

51 cognitive stages, cognitive processes, associative memory, MEG, functional connectivity,

52 synchronization, hidden Markov model, brain network, biophysical model, whole-brain model,

53 Kuramoto model

54

Introduction

56 Already in the 19th century, Donders hypothesized that information processing in the brain proceeds

57 through a sequence of fundamental cognitive stages with different functions such as visual

58 encoding, memory retrieval, and decision making [1]. Initially, cognitive stages were investigated

59 with behavioral metrics like reaction time (e.g., [2]). Over the past decade, neuroimaging analyses

60 have begun to uncover the neural correlates of these cognitive stages (e.g., [3]).

61

62 The dominant view is that cognitive stages require specific patterns of neural coordination across

63 the cortex [3–5]. The transition from one cognitive stage to the next is thought to be driven by the

64 basal-ganglia-thalamus (BGT) system which sets new states of cortical coordination [6–8]. The

65 striatum monitors the current state of the cortex, and based on a comparison to predefined states,

66 selects and triggers the next cognitive stage. The role of the BGT system modulating cortical

67 coordination is supported by animal studies, intracranial recordings, and neural models [9–14].

68 However, the network-level mechanisms required to reach a new state of cortical coordination from

69 subcortical inputs are poorly understood.

70

71

72 To give a detailed account of these mechanisms, one first needs to characterize the different states

73 of neural coordination within the sequence of cognitive stages. We measured neural activity with

3   3

74   cortically projected magnetoencephalographic (MEG) recordings as these have a sufficiently fine

75   temporal resolution to measure cognitive stages, as well as adequate spatial resolution. However,

76   cognitive stages have high temporal variability – that is, stages typically have a different duration

77   on each trial of an experimental task – which makes it difficult to measure neural coordination. To

78   overcome this problem, we used a machine learning method that identifies the onsets of cognitive

79   stages on a trial-by-trial basis [15]. Afterwards, the identified stage onsets were used to time-lock

80   the measures of neural coordination within regions (local synchrony) and between regions

81   (functional connectivity, FC), as there are concurrent changes at both spatial scales [16,17].

82

83   The machine learning method used to identify cognitive stages combines multivariate pattern

84   analysis with a Hidden semi-Markov Model (HSMM-MVPA). The HSMM-MVPA method searches

85   in each trial for a sequence of short-lived modulations of MEG amplitude (hereafter called *bumps*,

86   following the original paper [15]) that have a consistent topology across trials. These bumps signify

87   the onset of cognitive stages, and are thought to be triggered by the BGT system. Previously this

88   method has been used successfully to, for example, identify the cognitive stages that are affected by

89   task manipulations such as difficulty, stage insertion, and evidence accumulation for decisions

90   [4,5,15,18].

91

92   To understand how events from the BGT system can cause switches between states of neural

93   coordination – and thus between cognitive stages – we build upon generative whole-brain

94   biophysical models of large-scale activity (GWBM) that have been used to explain the dynamics of

95   neural coordination at rest [19]. GWBMs reduce the whole-brain network of neurons and synapses

96   to a smaller network that still incorporates the most relevant principles of neural dynamics. The

97   nodes of such a network describe the macroscopic activity within a region, while the links reflect

98   the neural fibers that connect these regions (i.e. structural connectivity).

99

4   4

100   GWBMs of resting state indicate that time-resolved patterns of neural coordination are related to the

101   anatomical structure of the brain and that these patterns evolve without requiring any input (a

102   phenomenon referred to as *metastable coordination*; [17,19]. Such coordination dynamics are

103   thought to provide an optimal mechanism for simultaneously integrating and segregating

104   information that allows the system to adapt quickly or alternatively, to persist in a given state [20].

105   While this is sufficient to explain resting-state data, cognitive tasks require specific, controlled

106   sequences of coordination states.

107

108   Here, we explored a GWBM in which inputs from the BGT system modulated local connectivity

109   strength briefly at the onset of cognitive stages, as suggested by cognitive theories and

110   electrophysiology measurements [6–14]. In other complex networks with similar dynamics as the

111   brain, such local perturbations can, in turn, produce controlled switches between global states [21].

112   Similarly, even though the inputs from the BGT system only triggered direct changes in local

113   connectivity strength, we observed transient modulations of local synchrony and switches to the

114   targeted states of directed functional connectivity that lasted until the next input. When there were

115   no further inputs from the BGT system, neural coordination returned to resting-state patterns after

116   tens of seconds. These results matched the observed neural coordination throughout the cognitive

117   stages in the empirical data. Finally, we used the GWBM to determine the importance of each brain

118   region in facilitating the switches between states of coordination.

119

Results

Five cognitive stages in an associative memory task.

122   We re-analyzed MEG data from an associative memory recognition task with 18 participants [3].

123   We chose this task because associative recognition memory involves a rich variety in cognitive

124 stages that have also been widely studied [3,5,15,22,23]. The task consisted of a self-directed

125 learning phase during which participants memorized 32 word pairs and a test phase. In the test

126 phase – which we analyzed here – participants were again presented with word pairs. These could

127 be *target* pairs from the learning phase or *re-paired foil* pairs, which consisted of the same words

128 paired differently (e.g., if the participants learned apple-tree and month-house, a foil pair could be

129 apple-house). Participants were asked to indicate as quickly and accurately as possible with a key

130 press if it was a learned pair or a re-paired foil. Only correct responses were included in our

131 analysis. We were interested in the evolution of neural coordination along with the cognitive stages

132 involved in performing the task, and in particular in how the brain switches between these

133 consecutive states of functional neural coordination.

134

135 As the goal is to develop a cortical model, the MEG signals were projected onto 5,124 cortical

136 sources using the structural MRI of each participant with minimum-norm estimation [3]. The

137 resulting cortical activity was parcellated and averaged into time-series for 68 cortical regions

138 following the Desikan-Killiany atlas [24]. Next, HSMM-MVPA was used to estimate the timing of

139 bumps that indicate the onset of cognitive stages in each trial. All trials were assumed to go through

140 the same sequence of stages as in previous studies [3,4,15]. Thus, bumps were assumed to have the

141 same spatial topology across trials, but trial-to-trial variable temporal location. Nevertheless, the

142 HSMM-MVPA can cope relatively well with extra bumps in some trials [15]. The intervals between

143 stimulus-onset-to-bump, bump-to-bump, and bump-to-response constitute the cognitive stages. A

144 leave-one-subject-out cross validation method showed that the MEG data were best explained by a

145 HSMM-MVPA model with four bumps, which corresponds to five cognitive stages (Figure 1A).

146

147 Following previous work on associative recognition [3,5,15], we interpreted the five cognitive

148 stages as follows: pre-encoding, encoding of visual information, memory retrieval, decision

149 making, and motor response. We did not analyze the pre-encoding stage as it is mostly driven by the

6   6

150 task stimulus and not by events from the BGT system that produce the transitions between cognitive

151 stages. The retrieval and motor stages were longer and had larger across-trial variability than the

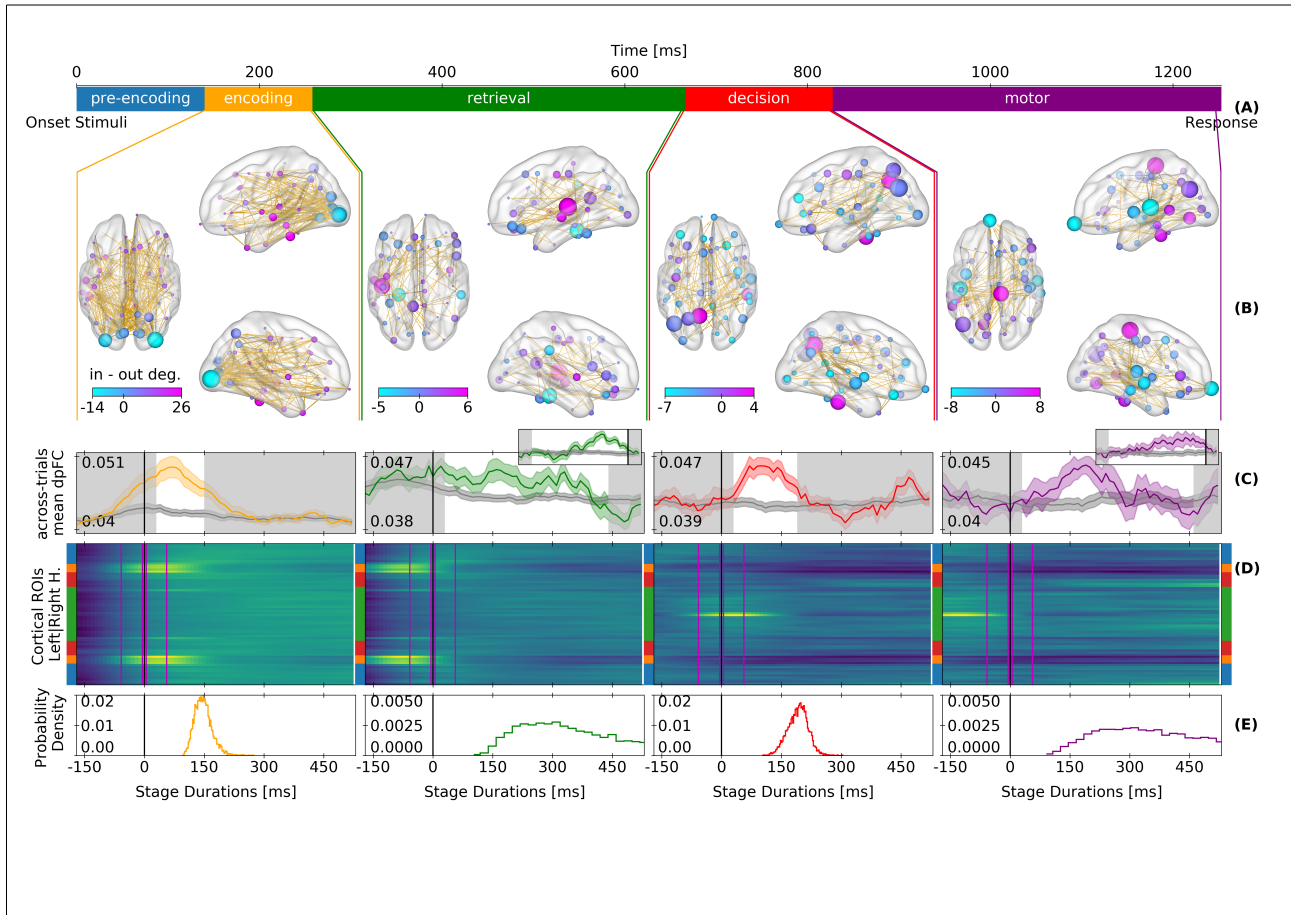152 encoding and decision stages (Figure 1A and E).

153

Figure 1. Theta-band MEG local synchrony and directed functional connectivity by cognitive stages. (A) Cognitive stages derived with the HSMM-MVPA along with their median durations. (B) Significant directed functional connectivity throughout the stage (*within-stage dpFC*). Links go from phase-ahead to phase-behind regions. The nodes represent the nodal degree (size) and the difference between phase-ahead and phase-behind links (color). (C) Directed functional connectivity time-locked at the onset of the stages (*across-trials dpFC*). Colored (dark gray) line: average across links with (without) significant across-trial dpFC at the current stage; Shading: standard error of the mean across subjects. Black horizontal lines are the onset of the stages. The

white background spans the median stage duration. Retrieval and response insets: Directed functional connectivity time-locked to the onsets of the decision stage and to the end-of-trial response, respectively (D) Across-trials averaged local synchrony (z-scored envelope of amplitudes) time-locked at the onset of the stages. Y-axis represents cortical regions – blue: temporal, orange: occipital, red: parietal, and green: frontal. Magenta lines: time windows to measure the relative change in local coordination at the onset of the stages. (E) Histogram of stage durations derived with the HSMM-MVPA.

154

Different local synchrony and directed functional connectivity states between stages.

Next, we measured neural coordination in the discovered stages. We focused on coordination of theta band oscillations (4-8 Hz), for several reasons: we previously found synchrony patterns inthis frequency band to vary across task stages [4]; theta oscillations have been related to cognitive processes such as attention, memory, control, and decision making [25–28]; the phase of theta oscillations is known to modulate the activity in higher frequency bands [26,29]; local modulations of theta-band activity are hypothesized to mediate changes in long-range functional connectivity [30]; and thalamic activity modulates cortical theta band activity [31].

164

Directed FC in the theta band was operationalized by means of the directed phase-lag index [32] (dpFC). A significant dpFC indicates that the phase in one region is consistently ahead or behind another region. The significance of dpFC was obtained using 200 surrogate data sets with random circular shifts of the original phases. We measured first *within-stage dpFC* to capture directed FC states that are constant from the start to the end of a cognitive stage. Figure 1B shows the links with significant within-stage dpFC, as well as the local difference between phase-ahead and phase-behind links (node color) and the total number of links regardless of their direction (node size).

8 8

172 Next, we measured *across-trial dpFC* of the significant links in a stage to reveal the temporal

173 evolution of directed FC during the stage (Figure 1C). Across-trial dpFC was calculated sample-by-

174 sample with the trials time-locked to the onset of each stage.

175

176 Across-trial dpFC revealed that functional states of directed FC switch at the transition between

177 cognitive stages. These switches are visible because across-trial dpFC takes into account the trial-

178 to-trial temporal variability of the cognitive stages as revealed by the HSMM-MVPA analysis. For

179 example, for the memory retrieval stage, across-trial dpFC seems to fade halfway through.

180 However, when across-trial dpFC is time-locked to the onset of the next stage – the decision stage –

181 dpFC for memory retrieval materializes until shortly before the decision stage (see the insets in

182 Figure 1). This illustrates why the HSMM-MVPA analysis is crucial: otherwise dpFC would appear

183 to fade quickly after stimulus onset, while that is not the case when first isolating cognitive stages.

184

185 Local synchrony was operationalized as the envelope of the theta band analytic signals in each

186 region, which indicates the degree of synchronous neural activity within a region. The envelopes

187 were z-scored over time and then averaged across trials and participants. Across-trial averages were

188 time-locked to the onset of cognitive stages which gave a time course of local synchrony for each

189 stage (Figure 1D). This showed that the local modulations of synchrony occurred only briefly at the

190 start of each stage, and involved different regions depending on the cognitive operations involved in

191 that stage.

192

193 As expected, each stage had a different neural coordination pattern. In the visual encoding stage,

194 occipital and left-temporal regions showed local synchrony and dpFC which might facilitate the

195 transfer of visual information to the medial temporal lobe and the hippocampus to start a retrieval

196 process [23]. The encoding of information is controlled by a large fronto-posterior, fronto-lateral

197 network [25,26]. During the memory retrieval stage, local synchrony at occipital and temporal

9   9

198 regions is reduced. dpFC now happens mostly between left-medial-temporal and frontal regions,

199 whose coordination is required for memory tasks [23,33]. At the onset of decision making the

200 frontal regions begin to synchronize locally. The decision process is mediated by fronto-parietal

201 dpFC [27], and dpFC between temporal and parietal regions dpFC to reinsert the memory retrieved

202 into the left-parietal cortex [23]. Finally, at the motor stage a large dpFC network appears between

203 motor, temporal, left-parietal, and pre-frontal regions. This complex network has previously been

204 associated with motor preparation, action reevaluation, decision, and cognitive control [27,28,34],

205 in line with the idea that the action is reevaluated during the motor response [35].

206

207 Together, these analyses unveiled that right at the onset of a cognitive stage there is a reorganization

208 of neural coordination in the cortex. Whereas the change in local synchrony was only brief, dpFC

209 lasted throughout the cognitive stage, indicating that short modulations of local synchrony can have

210 persistent global effects. Next, we used a GWBM to investigate the mechanism underlying this.

211 **Generative large-scale whole-brain model (GWBM)**

212 In order to integrate cognitive stages and neural coordination into one framework along with neural

213 anatomy and neural dynamics, we used a parsimonious GWBM that describes within- and between-

214 region modulations of synchrony. Previously, we have used this model to demonstrate that

215 modulations of local synchrony are related to time-resolved FC during resting state [17].

216

217 This GWBM is a low-dimensional reduction of a network-of-networks of Kuramoto oscillators

218 [36]. Kuramoto oscillators describe the dynamics of synchrony in biological systems including

219 neural networks [19,37,38]. Each sub-network represents a cortical region. All units in a region are

220 assumed to be fully and instantly connected, while connections between regions are weighted and

221 delayed by the density and length of the neural fibers in MRI-derived structural connectivity

10   10

222   networks. The regions in the GWBM were defined with the same parcellation atlas as the MEG data

223   that we sought to model.

224

225   First, we set default values for local connectivity strength (L in Eq. 2, identical for all regions), and

226   global scaling (G in Eq. 2 and Eq. 3) of the structural connectivity such that the model simulated

227   resting-state coordination dynamics in the theta-band [19,39]. Resting-state dynamics are

228   characterized by fluctuations over time of the local and global synchrony as well as time-resolved

229   FC patterns (i.e. local and global metastability) [17,19,39]. These dynamical properties of resting

230   state neural coordination were identified with GWBMs simulated over a grid of L and G values. The

231   identified L and G values displayed the most similar dynamics to local and global metastability in

232   the grid search.(see Supplementary Figure 1A).

233

234   Next, we simulated the switching between cognitive states by adding short inputs (30 milliseconds)

235   from the BGT system at the onset of cognitive stages. The rationale for using this mechanism

236   derives from theories of cognition and data derived from electrophysiology. Specifically, cognitive

237   theories state that the BGT system modulates cortical synchrony at the onset of cognitive stages via

238   thalamocortical signals [6,22]. Electrophysiology has shown that thalamocortical neurons can

239   indeed drive cortical activity [10,13] and establish FC [40,41]. These thalamocortical neurons tend

240   to produce short burst of activity [42], which target pools of either excitatory or inhibitory cortical

241   neurons specifically [12,43]. Therefore, our model simulated thalamocortical inputs as short pulses

242   of increased or decreased local connectivity strength (L in Eq. 2) that represent transient

243   modulations of excitatory or inhibitory synaptic activity [38].

244

245   To simulate the sequence of neural coordination states found in the MEG data, we estimated the

246   required activity pulses simultaneously in all regions, stage-by-stage. The optimization scheme

11   11

247 maximized concurrently the fitness of local synchrony and within-stage dpFC, while minimizing

248 the total magnitude of the pulses. The optimization was accomplished with the generalized island

249 model for distributed evolutionary optimization which in relatively short time explores and exploits

250 different areas of the parameter space simultaneously [44].

251

252 **Changes in local connectivity cause switches between global states of cognitive**

253 **coordination**

254 To assess how well the model simulated local synchrony, we measured the relative change in theta

255 envelope before and after stage onset (magenta lines in Figure 1D). All model results were

256 computed from 1000 models randomly selected from the top one percentile of models after the

257 optimization. Relative changes in simulated and MEG envelopes were correlated significantly

258 across different cortical regions (Spearman's ρ – encoding: 0.552 ± 0.00158 SEM; retrieval: 0.702

259 ± 0.000434 SEM; decision: 0.743 ± 0.000683 SEM; motor 0.477 ± 0.00151 SEM; all p-values <
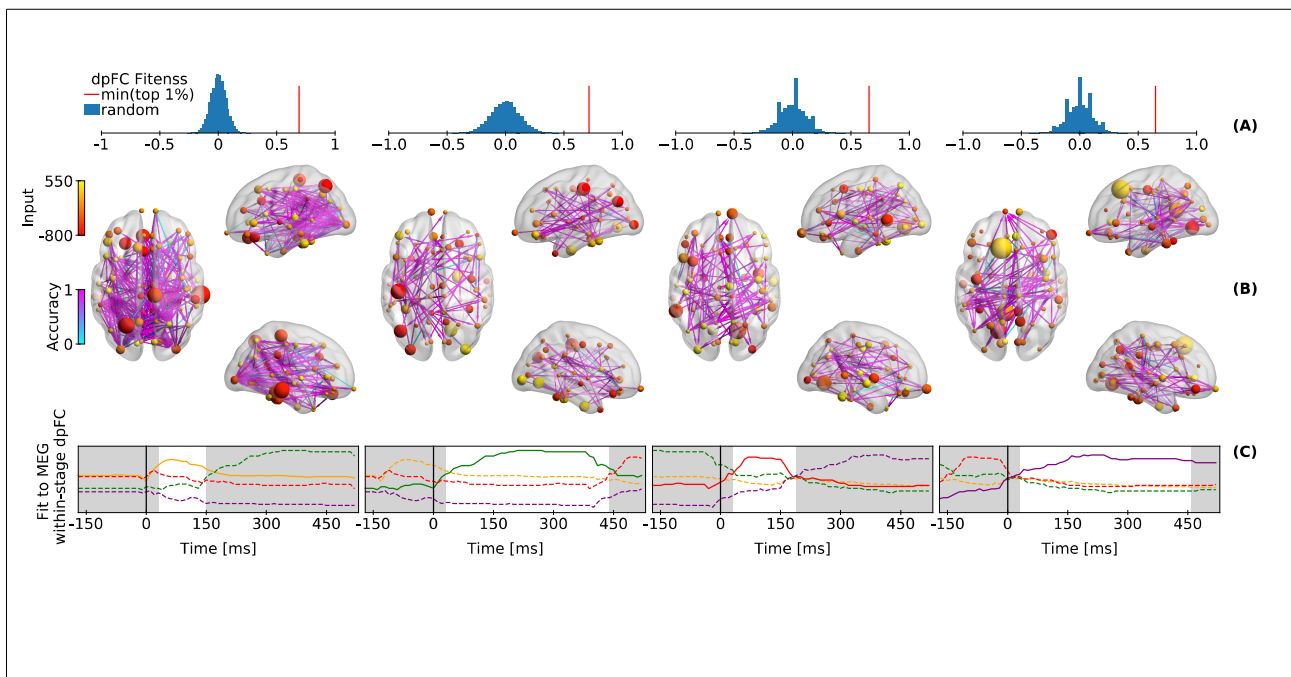
260 0.05).

261

Figure 2. Simulated directed functional connectivity. (A) Blue histograms show the fitness between 20,000 randomly generated *within-stage dpFCs* and the MEG *within-stage dpFC*. The red line indicates the *within-stage dpFCs* fitness of the model with the lowest fitness index within the top 1 percentile of the optimized models. (B) Fitness of simulated-to-MEG *within-stage dpFC* is shown in cyan-purple grading over MEG links with significant *within-stage dpFC* (same as Figure 1B). The nodes indicate the relevance of a region for reaching a state of within-stage dpFC (size), and the pulse of local connectivity strength at the onset of the stage due to sub-cortical inputs (colors). These results show the averages of 1000 random picks from top ~1% of the optimizations. (C) Temporal evolution of simulated-to-MEG fitness of *within-stage dpFC* for the current stages (solid lines) compared to other stages (dashed). The white background spans the median stage duration. The color of the lines represent the different stages and follows Figure 1C.

262

263 Figure 2A compares the within-stage dpFC fitness of the *worst* model in the top one percentile to a

264 distribution of the same fitness metric obtained with 20,000 random within-stage dpFCs, and shows

265 that the model performs much better than chance. Figure 2B shows the fitness of within-stage dpFC

266 at individual links. The fitness was quantified as the proportion of links with the same phase-lag

267 direction as in the MEG data (encoding: 0.697 ± 0.00014 SEM; retrieval: 0.837 ± 0.0016 SEM;

268 decision: 0.749 ± 0.00092 SEM; motor: 0.758 ± 0.001 SEM). Figure 2C compares the across-trial

269 dpFC of the model to the MEG data over time. Each state of dpFC begins after the pulse that

270 modulates local connectivity strength at the onset of the stage, and vanishes with the next onset

271 (Figure 2C). The last state of dpFC – the motor response – vanishes slowly (in ~10 seconds), and

272 the GWBM returns to resting-state coordination dynamics (Supplementary Figure 2).

273

274 Taken together, the GWBM showed that a short pulse of local connectivity strength at the onset of a

275 cognitive stage can first cause a modulation of local synchrony and then a new state of dpFC that

276 lasts until the onset of the next stage (Figure 2C). If there is no subsequent cognitive stage, the

277 GWBM returns to the coordination dynamics that are characteristic of the resting state.

278

279 **Relevance of regions to switch between functional states of coordination**

280 Not all regions in the GWBM are equally important for switching between states of dpFC. The

281 relevance of a region increases with the size of the pulses and the strength of structural connectivity

282 with other regions. The size of the nodes in Figure 2B indicates the relevance of a region for

283 switching between states of dpFC. The absolute size of the pulses from the BGT predicts 22.52 %

284 ($\pm$ 0.096 SEM) of the variance in the relevance of the nodes, while the interaction between the

285 absolute size of these BGT pulses and the log-scaled strength of structural connectivity predicts

286 25.98 % ($\pm$ 0.12 SEM) of the same variance.

287 This analysis shows that there are regions such as the left superior frontal region in the last stage

288 that do not show dpFC, but that are still highly relevant for entering a state of high dpFC between

289 other regions. This supports the mechanistic role of the superior frontal regions in exerting

290 cognitive control [25,27] and highlights the complexity of interactions required for implementing

291 changes in FC patterns.

292

293 **Discussion**

294 In this paper, we first analyzed the evolution of macroscopic neural coordination states across the

295 cortex during an associative recognition memory task. Our analysis of MEG data showed that at the

296 onset of fundamental cognitive stages there are transient modulations of local synchrony, which are

297 directly followed by a new state of dpFC that persists until the next cognitive stage. Next, we used a

298 generative model of whole brain activity (GWBM) with inputs from the basal-ganglia-thalamus

299 system to explain these findings. The GWBM showed that short pulses that strengthen or weaken

14   14

300   local connectivity strength at the onset of cognitive stages were sufficient to cause the switch

301   between states of neural coordination consistent with empirical data. In addition, the GWBM

302   indicated which individual regions were most relevant for causing these switches.

303

GWBM and the Basal Ganglia-Thalamus Circuit

305   The GWBM that we developed in this paper has shown that inputs from the basal-ganglia-thalamus

306   system at the onset of cognitive stages are sufficient to cause switches between cognitive stages.

307   This role of the BGT system had been hypothesized by cognitive theories [6,22]. Direct evidence

308   for thalamic modulations of cortical activity is limited to some cortical regions due to

309   methodological constraints, such as the fact that it is challenging to record simultaneously from

310   many sub-cortical and cortical areas with high temporal resolution [10,12,13,40]. Nevertheless, a

311   recent meta-analysis has shown that the thalamus plays a critical role as a central hub that connects

312   neighboring and distant regions to allow for cognitive functions [9], which is in line with the

313   hypothesis that local thalamocortical inputs can mediate FC [14]. In addition, there is evidence for

314   neural fibers connecting the thalamus with most cortical regions [45]. Our model provides

315   additional support for both hypotheses: the BGT systems can trigger a switch between fundamental

316   stages of cognition [6,22] and thalamic input modulates coordination of cortical activity according

317   to cognitive demands [14].

318

319   Given our limited understanding of how the thalamus modulates cortical activity, we opted for a

320   very simple representation of thalamocortical input. These inputs were short [40–42], targeted

321   excitatory or inhibitory local connections [12,43], and came at the onset of cognitive stages [6,22].

322   Such inputs drove the GWBM throughout the sequence of empirical local synchrony and dpFC

323   states. Afterwards, the GWBM returned to resting state dynamics. In other words, a short

324 modulation of local excitation/inhibition modified the local synchrony and the phase of the local

325 mean-field oscillation. This change in local mean-field phase set a new phase-lag relationship with

326 other regions that vanished over time due to structural cortical interactions. This response to local

327 perturbations suggests that cortical dynamics are metastable as many states of coordination can be

328 reached, and the brain does not remain into a particular state in the absence of perturbations.

329 Metastable dynamics are thought to allow for integrating and segregating information

330 simultaneously, as well as for the flexibility of cognitive functions and behaviors [20].

331

332 Importantly, dpFC was not driven by thalamocortical inputs exclusively. Instead, the macroscopic

333 connectivity structure of the brain also played an important role. The relevance of the structural

334 connectivity was highlighted by the presence of regions with very low dpFC that turn out to be very

335 important for coordinating other pairs of regions. One example of such regions is the left superior

336 frontal region during the motor response stage, a region that has been related to cognitive control,

337 attention, and decision making [25,27,28]. The role of structural connectivity for generating specific

338 coordination patterns was first brought to light by GWBMs of resting-state dynamics [19]. In a

339 previous study we have shown analytically that the strength of structural connectivity plays an

340 important role in selectively coordinating regions by means of modulations of local connectivity

341 strength [46]. Additionally, structural symmetries and time-delays might have influenced dpFC in

342 our simulations [19,47,48].

343

344 There are other biological aspects that might be relevant for coordination of cortical activity that

345 were not included here, including the delay over thalamocortical neurons [49], the dynamics of the

346 synapses targeted by thalamocortical inputs [12], tonic activity in the thalamus [42], noise, or the

347 state of cortical oscillations at the time of a thalamic input. Moreover, our measurement of directed

348 FC has neglected zero-phase-lag coordination which can emerge from thalamocortical and cortico-

349 cortical loops [49]. However, while including these additional aspects might improve the fit of the

350 model, the current model could already account for the data surprisingly well. Additionally, we have

351 assumed that perturbations of cortical dynamics at the onset of cognitive stages come exclusively

352 from the thalamus. However, there might be other regions such as the hypothalamus that modulate

353 cortical activity in the same or another way that is not included in our model.

354

355 **Neural coordination across the cortex along a sequence of cognitive stages**

356 Our stage-by-stage analyses of neural coordination corroborates the hypothesis that the local

357 modulations of phase synchrony in the theta-band mark a change in long-range functional

358 connectivity and enable a new cognitive function [30]. Moreover, our results confirm the hypothesis

359 that a new state of neural coordination is established at the onset of cognitive stages [6,22]. Our

360 previous research has shown that alpha band FC also varies across cognitive stages [4], but cortical

361 alpha has been found to lead thalamic activity rather than being caused by it [50], as is the case with

362 theta [13].

363

364 To uncover neural coordination stage-by-stage it was crucial to account for the temporal variability

365 of cognitive stages across trials using the HsMM-MVPA analysis. Only after correcting for this

366 variability, our analyses showed that dpFC lasts throughout a cognitive stage and differs across

367 stages. The corresponding states of dpFC had different length, strength, and topology. This diversity

368 of properties might have biased some traditional metrics of neural coordination. For example, if one

369 were interested in the FC at the interval between 250 and 600 milliseconds after stimulus onset –

370 roughly the period of memory retrieval, this interval would contain elements of the encoding or

371 decision stages. The first reason for this is the trial-by-trial variability in stage durations: in one trial

372 encoding might last till 400 ms, while in another trial memory retrieval might already have finished

373 by 400 ms. Secondly, the retrieval stage has fewer and weaker connections than the encoding and

374 decision stages in our study, which mean that these connections might have been missed altogether.

375 These effects are worse the further one moves away from fixed time points (trial onset/response),

376 which is one of the reasons that M/EEG studies have had severely limited trial lengths traditionally.

377

378 Furthermore, our stage-by-stage analysis might contribute to disentangling competing theories. For

379 example, our results suggest that the decision is made and evaluated in the last two stages. We

380 interpreted the penultimate stage as a decision process in which memories are transferred to parietal

381 areas by coordinating left-temporal regions with parietal regions, mediated by local frontal and

382 fronto-parietal coordination [15,23,25,27]. The last stage has been traditionally related with a pure

383 motor response. However, our results indicate that the motor stage has elements associated with

384 motor preparation, action reevaluation, decision, and cognitive control [26,28,34]. This functional

385 network in the last stage suggests that during the motor stage the decision is reevaluated, and it

386 supports the line of thought in which responding is a process that is not independent from decision

387 making (e.g., [28,35]).

388

389 **Conclusion**

390 To the best of our knowledge we have developed the first generative large-scale brain model that

391 simulates the dynamics of the states of neural coordination along the fundamental cognitive stages

392 in a task. In this model we have integrated structural connectivity, macroscopic neural dynamics,

393 sub-cortical inputs, and the cognitive theories of associative recognition memory. The model has

394 multiple simplifying assumptions which made it feasible to simulate and optimize the model while

395 taking into account the macroscopic properties of neural anatomy and dynamics. This work opens

396 up the way for considering other tasks in similarly integrated and multidimensional manners to

397 better understand how the brain implements cognition through cortical coordination.

398

Methods

Experimental paradigm

401 We re-analyzed MEG data from an associative memory task [3]. We combined the trials with

402 correct responses from all experimental conditions, as we were interested in the transition between

403 fundamental cognitive stages and not in the differences between conditions (which did all proceed

404 through the same stages; [15]). All 18 participants were right handed (6 males and 12 females with a

405 mean age of 23.6 years).

406

407 First, participants studied 32 pairs of words until they knew them well [3]. This was followed by a

408 test session in which MEG was recorded. In the test session participants were presented with pairs

409 of words which were either the same as in the study season (*targets*) or paired differently (*re-paired*

410 *foils*). The pairs of words remained on the screen until the participant responded, and were followed

411 by 1-sec feedback and a brief inter-trial interval. A full description of the task and the recording

412 procedure can be found in [3].

413

MEG data preprocessing

415 MEG data was preprocessed and source-reconstructed following the analysis pipeline of the original

416 manuscript [3]. After artifact rejection there were 6,708 trials left. The MEG data of each participant

417 was combined with their own structural MRI to obtain the cortical sources of MEG data. MEG

418 sources consisted of 5,024 dipoles estimated with cortically constrained minimum norm estimates

19   19

419   [3,51]. Source estimates were then morphed onto the standard MNI brain and parcellated into 68

420   cortical regions with the Desikan-Killiany atlas [24,52]. Each parcel contained the average activity

421   of all dipoles within the region with a 100 Hz sampling rate.

422

423   **Identification of cognitive stages**

424   To find the onset of cognitive stages the data were bandpass filtered (1-30 Hz, which are default

425   values in Field Trip [53]) and epoched from trial onset to response. Single trials were baseline

426   corrected (-0.4 to 0 seconds), and transformed to one covariance matrix per subject. The average

427   covariance matrix across subjects was used to reduce the dimensionality of the data to 33 principal

428   components (which together accounted for 90 % of variance). These principal components were z-

429   scored and fed into the HSMM-MVPA. The HSMM-MVPA first applies a half-sine window

430   function to increase the signal-to-noise ratio of the *bumps,* the cortical response to sub-cortical

431   input. The bumps are assumed to be 50-millisecond modulations of amplitude at the onset of

432   cognitive stages with the same topology across trials. The signals from the end of a bump to the

433   next bump are assumed to have zero-mean amplitude, a *flat*. The duration of a given stage (bump +

434   flat) is assumed to come from a gamma distribution with shape parameter equal to two.

435   Consequently, a stage is modeled as a bump of a certain amplitude followed by a zero-mean

436   amplitude flat and a duration given by a gamma-2 distribution. There is one exception and this is

437   the first stage (pre-visual encoding here) which does not start with a bump. With this stage model

438   and a predefined number of stages, the Baum-Welch algorithm for HSMMs searches the amplitude

439   and location of bumps that explain the z-scored principal components best [54]. The bump

440   amplitudes (for the 33 PCA components) are the same for all trials and vary across stages. The

441   temporal location of the bumps also varies across trials, but the resulting stage durations are

442   constrained to gamma-2 distributions with one scale parameter per stage.

443

444   We explored models with 3 to 7 cognitive stages as previous studies have shown that this memory

445   task consists of 5 to 6 stages [4,5,15]. For each model we ran the HSMM-MVPA 200 times with

446   random initial parameters to avoid converging in local maxima. We used a leave-one-subject-out

447   cross-validation to assess whether a model with *N+1* stages could explain the data significantly

448   better (using a sign-test) than a model with *N* stages [15]. The final model was the simplest one that

449   generalized across subjects – a five-stage model. Then, we allowed one stage to have different

450   gamma-scale parameters across experimental conditions, and we used leave-one-subject-out cross-

451   validation to decide on the best model. As in previous studies [4,15], a model with different gamma

452   distributions in the retrieval stage explained the MEG data best.

453

Measurements of neural coordination

455   To measure neural coordination – local synchrony and directed functional connectivity – we used

456   the analytic signal of theta band oscillations. The parcellated MEG data were band pass filtered

457   (cut-off frequencies: 3.8, and 8.5 Hz; forward-backward IIR Butterworth filter of order 4) and

458   epoched from -0.4 seconds before stimulus onset to 0.4 seconds after the response. Epochs were

459   Hilbert transformed to the analytic signal using a symmetric padding of 0.4 seconds to avoid edge

460   artifacts.

461

462   Directed functional connectivity between regions *i* and *j* was measured with the directed phase-lag

463   index (dpFC) [32] as follows:

464

465   $$dpFC^{ij} = \frac{1}{N} \sum_{n=1}^{N} \frac{1}{T_n} \sum_{t=s+1}^{s+T_n} sgn\left(\operatorname{Im}\left(S_{nt}^{ij}\right)\right) \qquad \text{Eq. 1}$$

466

21   21

467 In Eq. 1, *Im(S^{ij})* is the imaginary part of the cross-spectral density, and *sgn* is the sign function. To

468 compute within-stage dpFC, *s+1* was the first sample 0.05 seconds after the onset of the stage, *Tn*

469 was the length of the stage in trial *n*, and *N* is the number of trials. Across-trials dpFC was

470 computed sample-by-sample with *Tn = 1* and time-locked to stage onset. Both within-stage and

471 across-trial dpFC were later averaged across subjects. A detailed explanation can be found in the SI.

472

473 **Generative whole-brain model**

474 The generative whole-brain model (GWBM) was derived with the Ott-Antonsen ansatz [55] from a

475 network-of-networks of Kuramoto oscillators [36]. See [17] for a step-by-step derivation. The

476 dynamics of synchrony in a region are given by the Kuramoto order parameter (KOP) which

477 describes the dynamics of synchrony in in biological systems as well as a pool of neurons [56]. The

478 KOP is a complex number $\left(KOP=r\,e^{i\psi}\right)$ with the modulus bound by zero (asynchrony) and one

479 (full synchrony). Here, the KOP simulated the analytic signal of the MEG data. Beforehand we set

480 the natural frequencies of the oscillators to a Lorentzian distribution centered in the theta band

481 (center, *Ω*: 6 Hz, spread, *Δ*: 1), and the spike-propagation velocity along the structural fibers to 5

482 m/s. The equations of the KOP in on region, *i*, of the GWBM are as follows:

483

484 $$\dot{r}_i = -\Delta_i r_i + \frac{L_i}{2}(1-r_i^2)r_i + \frac{G}{2R}(1-r_i^2)\sum_{j=1, j \neq i}^{R} A_{ij} r_j\left(t-\tau_{ij}\right)\cos\left(\psi_j\left(t-\tau_{ij}\right)-\psi_i\right) \qquad \text{Eq. 2}$$

485 $$\dot{\psi}_i = \Omega_i + \frac{G}{2R}\left(r_i+\frac{1}{r_i}\right)\sum_{j=1, j \neq i}^{R} A_{ij} r_j\left(t-\tau_{ij}\right)\sin\left(\psi_j\left(t-\tau_{ij}\right)-\psi_i\right) \qquad \text{Eq. 3}$$

486

487 The time dependency has been removed in variables without time delays; *τ* are the time delays

488 between regions (fiber length x spike-propagation velocity); *A* is the coupling strength between

22   22

489 regions (density of structural fibers); and R is the number of regions. To simulate resting state

490 dynamics we explored parameters G (global scaling of structural connectivity) and L (local

491 connectivity strength, same in all regions) with 25 randomly initialized models. The results of this

492 exploration are shown in SI Figure 1. With G and L set to correctly reproducing the resting state, the

493 thalamocortical inputs were simulated as 0.03 second increases/decreases of L at each region and

494 stage onset independently. Simulated dpFC was measured with Eq. 1, but here N represented 25

495 models with different initial conditions and T_n was the median duration of the MEG stages. The

496 initial conditions for the first stage were the MEG phases and amplitudes at the pre-encoding stage

497 plus random noise. More details of the simulations are reported in the SI.

498

Generative whole-brain model: Resting-state

500 To identify a GWBM that simulated resting-state dynamics we performed a grid-search over the

501 global and local coupling parameter space. The local couplings were assumed to be identical for all

502 regions. Resting-state dynamics are characterized by temporal fluctuations of global and local

503 synchrony, and time-resolved patterns of functional connectivity (i.e. metastable dynamics).

504 Metastability was measured as the standard deviation of the modulus of the KOP over time at local

505 and global levels [57,58]. At the local level, the metastabilities were averaged across regions. To

506 obtain the global KOP over time we averaged the phases of the local KOPs across regions (ψ in

507 Equation 3 of the main text). To assess the temporal structure of the global metastability we

508 computed the mean of the absolute values of its autocorrelation function. To avoid the influence of

509 the initial conditions on the simulations we ran twenty-five GWBMs with random initial conditions

510 for each combination of parameters. The simulations were run for 1000 seconds, but the initial 200

511 seconds were removed to discard initial transients. All simulations were performed with a time-

512 delayed first-order Euler method and an integration step of 1 millisecond. We ended up with a

513 global coupling of 0.15 and a local coupling of 0.7, which had the best trade-off between high

23 23

514 metastability and low autocorrelation of global KOP, and therefore were chosen as the default

515 values for the following GWBMs. Supplementary Figure 1 shows the grid search results of resting-

516 state dynamics.

517

518 **Generative whole-brain model: cognitive task**

519 To simulate the sequence of cognitive stages and their associated neural coordination patterns, we

520 initialized 25 models informed by the theta-band phases and envelope amplitudes observed at the

521 pre-encoding stage. The MEG envelopes were measured 0.1 and 0.05 seconds before the onset of

522 the encoding stage. Then, the initial history of the KOP modulus was a straight line that joined the

523 mean of these amplitudes across trials plus Gaussian noise (σ=0.01). To choose the initial history of

524 phases we measured inter-trial phase consistency, and within-stage dpFC at the pre-encoding stage.

525 There were 10 regions (mostly occipital and parietal) that showed significant inter-trial phase

526 consistency. The initial history of phases at these regions were set to the average MEG phases

527 across trials at 0.05 seconds before the onset of the first stage plus Gaussian noise (σ=0.01). The

528 phases of these regions were used as a referent point for the remaining regions. The initial phases of

529 the remaining regions were set by an optimization algorithm (CMAES [59]) which tried to establish

530 a phase-lag relationship between regions as in the empirical within-stage dpFC. The dpFC of the

531 initial history of phases had an average similarity to empirical within-stage dpFC of 78%. The 25

532 GWBMs of the later stages were initialized with the last simulated samples of the previous stage in

533 the best individual of the optimization process (see section *Optimization of thalamocortical inputs*).

534

535 The model with the best fitting sequence of parameters was left to run 400 seconds after the last

536 stage. Supplementary Figure 2 shows that the model neither remained trapped into the functional

537 connectivity state of the last stage, nor did it return to any of the previous states (SI Fig. 2, bottom).

24   24

538 Instead, the model returned to resting state patterns of global and local synchrony for which the

539 functional connectivity fluctuated over time (i.e. metastable dynamics; SI Fig. 2, top & middle).

540

Optimization of thalamocortical inputs

542 To find the optimal thalamocortical inputs for reproducing the observed connectivity patterns, we

543 used the generalized island model for evolutionary optimization [44] – algorithm DE1220 as

544 implemented in the pagmo toolbox [60]. The generalized island model optimized in parallel ten

545 islands connected in a ring. Each island consisted of 50 individuals and had a particular

546 parametrization of a differential evolution algorithm (see *Supplementary Table 1*). The islands

547 occasionally exchanged their best-fitted individuals. This configuration allowed for simultaneously

548 exploring and exploiting multiple areas of the parameter space. Their fitness function had three

549 objectives that were combined into one index of fitness. The dominant objective was to maximize

550 the similarity of simulated and empirical within-stage dpFC, f_1:

551

552 $$ f_1 \ = \ \sum_{i=1}^{E} x_i \cdot y_i \left(\sum_{i=1}^{E} |x_i| \right)^{-1} \qquad \text{Eq. 4} $$

553

554 The links, E, in the empirical dpFC, x, were either 0 (not significant), 1 (lag-ahead) or -1 (lag-

555 behind). Simulated dpFC links, y, were either -1 or 1. The objective f_1 gave discrete values which

556 interval was used by the other two objectives. The second objective, f_2, maximized the topological

557 similarity of the relative change in envelope amplitude at the onset of each stage. This similarity

558 was measured with the Spearman rank-correlation between MEG and simulated relative amplitudes.

559 The third objective, f_3, minimized the absolute size of the thalamic pulses as

560

561 $$f_3 = \frac{1}{L_{max}} \sum_{j=1}^{R} |L_j| \left(\sum_{i=1}^{E} |x_i| \right)^{-1} \qquad \text{Eq. 5}$$

562

563 where L_i are the local connectivities, and L_{max} is the largest absolute pulse allowed to the optimizers.

564 The combined fitness index was $f = f_1 - (1-f_2)f_3$. The best individual had the minimal $(1-f_2)f_3$ among

565 the 5000 individuals with the highest f in order to avoid a GWBM with low f_2 and f_3. The last

566 simulated samples of this individual were used to initialize the simulations of the next stage (see

567 section *Generative whole-brain model: Cognitive task*).

568

569 Supplementary Figure 3 shows the parameters of the individuals and their fitness along the

570 evolution in one island as example. This figure shows how the cost function could simultaneously

571 maximize the fitness of within-stage dpFC and relative local synchrony at the onset (Spearman

572 correlation), while the change in local coupling was minimized. The optimization of the four stages

573 took approximately 4 days using 10 CPUs, one for each island.

574

575 **Relevance of individual regions for switches**

576 To assess the relevance of a region for switching between states of dpFC, a GWBM was lesioned by

577 setting the thalamocortical pulse in this region to zero while the remaining regions were left

578 untouched. Then, the fitness of the lesioned GWBM (Eq. 4) was compared to the fitness achieved

579 by the original GWBM. The relevance of a region was measured as the number of within-stage

580 dpFC links in the lesioned model that were not matching MEG data relative to the number of links

581 matching MEG data in the full model. This process for measuring relevance was repeated for the 68

582 regions in the GWBM and the four transitions between stages. To obtain a measure of relevance that

583 was not dependent on a single GWBM, relevance was evaluated in 1,000 GWBMs randomly picked

584 from among the models in the top one percentile after optimization. Next, we used linear regions

26   26

585 models with one independent variable to explain the relevance of regions. Each linear model

586 included as dependent variable the relevance of the 68 regions and four stages in a lesioned

587 GWBM. A linear model was fitted for each of the 1,000 lesioned models independently.

588

589 **Structural connectivity, MRI acquisition and processing**

590 We used 45 subjects from the test-retest dataset of the Human Connectome Project (HCP) 3T. This

591 data set consisted of T1-weighted and multi-shell diffusion MRI data. T1-weighted data were

592 acquired with 0.7 mm isotropic voxel size, TE = 2.14 ms, and TR = 2400 ms. Diffusion MRI data

593 were acquired with a 1.25-mm isotropic voxel size, TE = 89.5 ms, and TR 5520 ms, with three

594 shells with b = 1000, 2000, and 3000 s/mm^2, each shell with 90 diffusion weighted volumes and 6

595 non-weighted images [61]. The diffusion MRI data was already preprocessed as described in [62].

596 In short, diffusion MRI data were corrected for head motion and geometrical distortions arising

597 from eddy currents and susceptibility artifacts [63]. Finally, the diffusion MRI images were aligned

598 to the structural T1 image. The T1w image was parcellated using the Desikan–Killany parcellation

599 [24], resulting in 68 cortical ROIs. Using the T1w image, the probability maps of the different

600 tissues were obtained to create the five tissue-type files [64,65].

601

602 Tractography was carried out with constrained spherical deconvolution [66,67]. A multi-tissue re-

603 sponse function was calculated [68] and the average response functions were calculated. The multi-

604 tissue fiber orientation distribution was calculated [69] with the average response function (L_{max} =

605 8). The fiber orientation distribution images had a joint bias field correction and a multi-tissue in-

606 formed log-domain intensity normalization [70]. Then, tractography was performed with the iFOD2

607 algorithm [71] using anatomically constrained tractography [72]; generating 10 million streamlines

608 (cutoff at 0.05, default); and using backtracking [72] and a dynamic seeding [73]. The length of the

609 fibers was set to a minimum of 20 mm and a maximum of 250 mm [72]. To be able to quantitatively

610 assess the connectivity, SIFT2 was applied to the resulting tractograms [73].

611

612 The connectivity matrix was built with a robust approach. In particular a 2-mm radial search at the

613 end of the streamline was performed to allow the tracts to reach the gray matter parcellation [74].

614 Each connectivity matrix was multiplied by its μ coefficient obtained from the SIFT2 process, as the

615 sum of the streamline weights needs to be proportional to the units of fiber density for each subject

616 [75]. Connectivity matrices were averaged across subjects, and the 10% of links with the highest

617 coefficient of variation across subjects were set to zero[76]. Finally, the averaged and thresholded

618 structural connectivity matrix was normalized to have an average value of one.

619

Supplementary Information

621 **Supplementary Table 1.** *Parameters of DE1220 algorithm on each island.*

Island IDs	Mutation variants allowed	Adaptation scheme for parameters F and C
1	best/1/exp; rand-to-best/1/exp; best/1/bin; rand-to-best/1/bin	jDE
2	rand-to-current/2/exp; rand-to-current/2/bin	jDE
3	rand-to-current/2/exp; rand-to-current/2/bin	iDE
4	best/1/exp; rand-to-best/1/exp; best/1/bin; rand-to-best/1/bin	iDE
5	rand/1/exp; rand/1/bin	jDE
6	rand-to-current/2/exp; rand-to-current/2/bin	jDE
7	rand-to-current/2/exp; rand-to-current/2/bin	iDE
8	best/1/exp; rand-to-best/1/exp; best/1/bin; rand-to-best/1/bin	jDE
9	best/1/exp; rand-to-best/1/exp; best/1/bin; rand-to-best/1/bin	iDE
10	rand/1/exp; rand/1/bin	jDE

622

623

624

625   **Supplementary Figures**
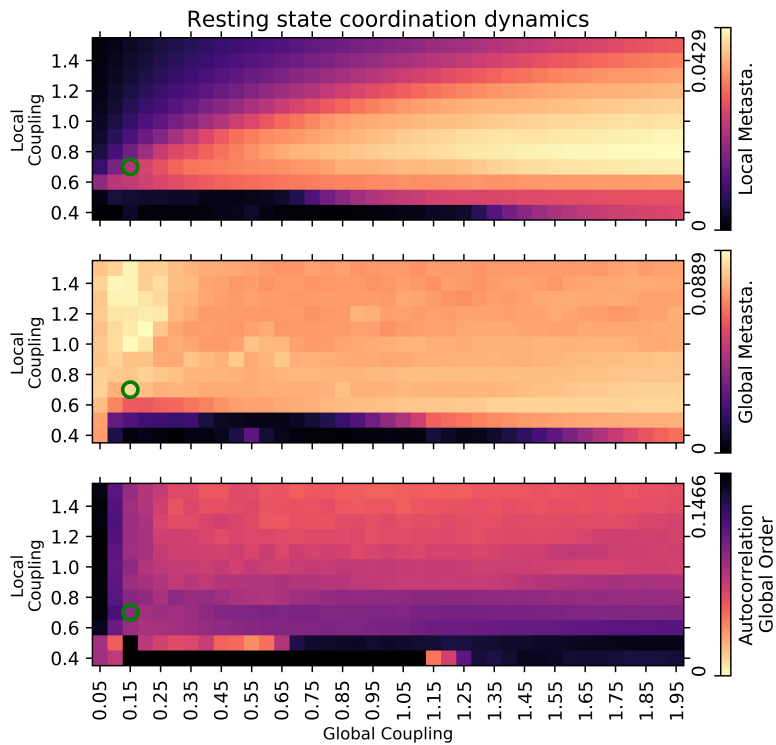
626

627

Figure S1, Resting state neural coordination dynamics. The green dot indicates the parametrization of the model. The location of the green dot was based on the idea that resting state dynamics should have simultaneously the lightest color in the three panels and the weakest coupling parameters.
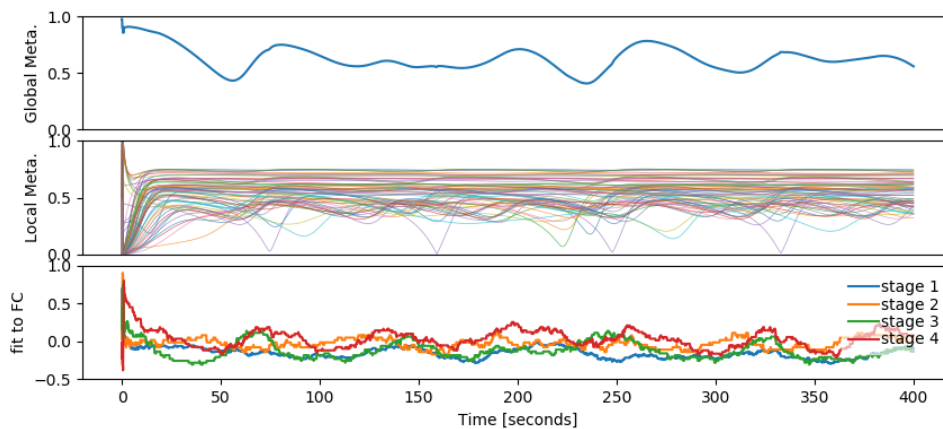
Figure S2. Return to resting-state after cognitive stages. (top) Modulus of the global KOP. (middle) Modulus of the local Kuramoto order parameter (KOP) for the cortical 68 ROIs. (bottom) Temporal evolution of simulated-to-MEG fitness of *within-stage dpFC* for the four cognitive stages. This is similar to Figure 2B but for a much longer period of time. The MEG *within-stage dpFC* of each stage (Figure 1B) were compared (Eq. 4) with the simulated *dpFC* sample-by-sample (Eq. 1).
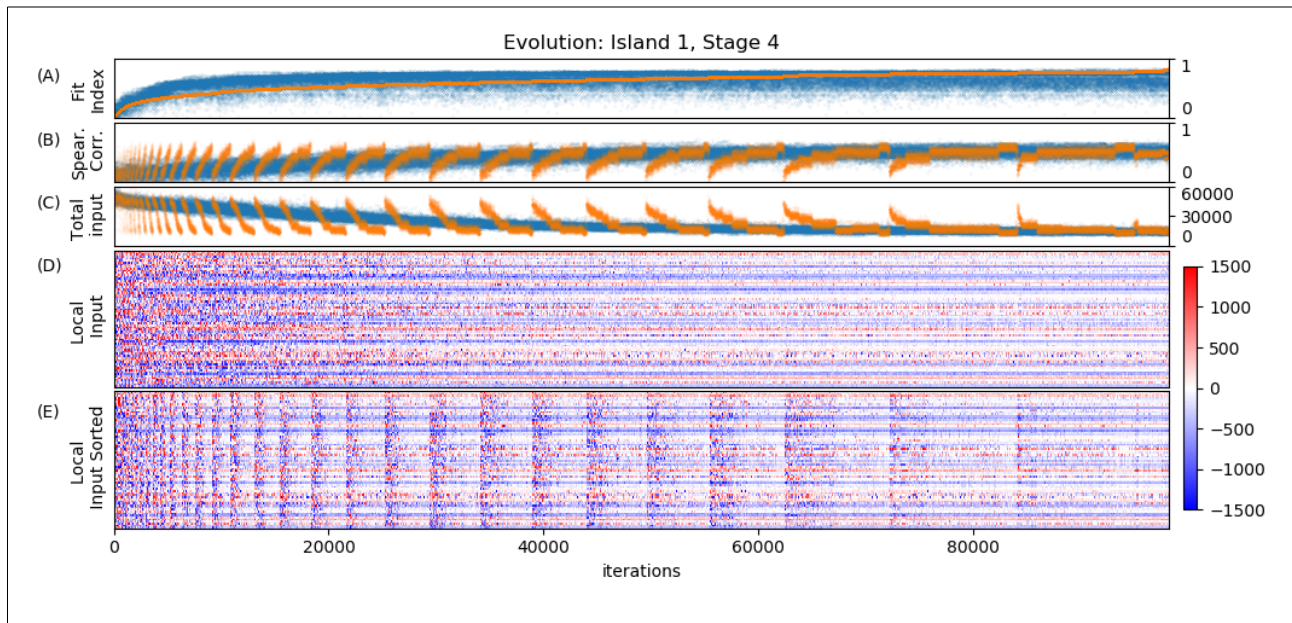
628

629

Figure S3. Individuals and their fitness along the optimization in one island. (A) fitness index f. (B) Spearman correlation, objective f_1. (C) Sum of the absolute change in local coupling at the onset of the stage. Blue dots are the A, B and C values in the order that they were evaluated along the optimization process. Orange dots are the same values but sorted by the Fit Index (A). (D) Change in local coupling (thalamic input) at the onset that produces the blue dots in A, B, C. (E) Same as (D) but sorted by their Fit Index.

630

631

Acknowledgments

Author contributions

Oscar Portoles: Designed research, Performed research, Analysed data, Wrote the paper

Manuel Blesa: Analysed and wrote structural data processing

Marieke van Vugt: Contributed in writing

Ming Cao: Contributed in writing

Jelmer P. Borst: Designed research, Wrote the paper

Competing Interests

The authors declare no conflict of interest

References

1. Donders FC. On the speed of mental processes. Acta Psychol (Ams). 1969;30: 412–431. doi:10.1016/0001-6918(69)90065-1

2. Sternberg S. The discovery of processing stages: Extensions of Donders' method. Acta Psychologica. 1969;30: 276–315. doi:10.1016/0001-6918(69)90055-9

3. Borst JP, Ghuman AS, Anderson JR. Tracking cognitive processing stages with MEG: A spatio-temporal model of associative recognition in the brain. NeuroImage. 2016;141: 416–430. doi:10.1016/j.neuroimage.2016.08.002

4. Portoles O, Borst JP, van Vugt MK. Characterizing synchrony patterns across cognitive task stages of associative recognition memory. Eur J Neurosci. 2018;48: 2759–2769. doi:10.1111/ejn.13817

5. Anderson JR, Borst JP, Fincham JM, Ghuman AS, Tenison C, Zhang Q. The Common Time Course of Memory Processes Revealed. Psychol Sci. 2018;29: 1463–1474. doi:10.1177/0956797618774526

6. Stocco A, Lebiere C, Anderson JR. Conditional routing of information to the cortex: A model of the basal ganglia's role in cognitive coordination. Psychol Rev. 2010;117: 541–574. doi:10.1037/a0019077

7. O'Reilly RC, Frank MJ. Making working memory work: a computational model of learning in the prefrontal cortex and basal ganglia. Neural Comput. 2006;18: 283–328. doi:10.1162/089976606775093909

8. Redgrave P, Prescott TJ, Gurney K. The basal ganglia: a vertebrate solution to the selection problem? Neuroscience. 1999;89: 1009–1023. doi:10.1016/s0306-4522(98)00319-4

9. Hwang K, Bertolero MA, Liu WB, D'Esposito M. The Human Thalamus Is an Integrative Hub for Functional Brain Networks. J Neurosci. 2017;37: 5594–5607. doi:10.1523/JNEUROSCI.0067-17.2017

10. Bruno RM, Sakmann B. Cortex Is Driven by Weak but Synchronously Active Thalamocortical Synapses. Science. 2006;312: 1622–1627. doi:10.1126/science.1124593

11. Rektor I, Bareš M, Brázdil M, Kaňovský P, Rektorová I, Sochůrková D, et al. Cognitive- and movement-related potentials recorded in the human basal ganglia. Mov Disord. 2005;20: 562–568. doi:https://doi.org/10.1002/mds.20368

12. Cruikshank SJ, Lewis TJ, Connors BW. Synaptic basis for intense thalamocortical activation of feedforward inhibitory cells in neocortex. Nat Neurosci. 2007;10: 462–468. doi:10.1038/nn1861

13. Malekmohammadi M, Elias WJ, Pouratian N. Human thalamus regulates cortical activity via spatially specific and structurally constrained phase-amplitude coupling. Cereb Cortex. 2015;25: 1618–1628. doi:10.1093/cercor/bht358

14. Saalmann YB. Intralaminar and medial thalamic influence on cortical synchrony, information transmission and cognition. Front Syst Neurosci. 2014;8. doi:10.3389/fnsys.2014.00083

15. Anderson JR, Zhang Q, Borst JP, Walsh MM. The discovery of processing stages: Extension of Sternberg's method. Psychol Rev. 2016;123: 481–509. doi:10.1037/rev0000030

16. Tewarie P, Hunt BAE, O'Neill GC, Byrne A, Aquino K, Bauer M, et al. Relationships Between Neuronal Oscillatory Amplitude and Dynamic Functional Connectivity. Cerebral Cortex. 2019;29: 2668–2681. doi:10.1093/cercor/bhy136

17. Portoles O, Qin Y, Hadida J, Woolrich M, Cao M, Vugt M van. Modulations of local synchrony over time lead to resting-state functional connectivity in a parsimonious large-scale brain model. bioRxiv. 2021; 2021.01.20.427443. doi:10.1101/2021.01.20.427443

18. Zhang Q, Walsh MM, Anderson JR. The Impact of Inserting an Additional Mental Process. Comput Brain Behav. 2018;1: 22–35. doi:10.1007/s42113-018-0002-8

19. Cabral J, Kringelbach ML, Deco G. Functional connectivity dynamically evolves on multiple time-scales over a static structural connectome: Models and mechanisms. NeuroImage. 2017;160: 84–96. doi:10.1016/j.neuroimage.2017.03.045

20. Tognoli E, Kelso JAS. The Metastable Brain. Neuron. 2014;81: 35–48. doi:10.1016/j.neuron.2013.12.022

21. Wang L-Z, Su R-Q, Huang Z-G, Wang X, Wang W-X, Grebogi C, et al. A geometrical approach to control and controllability of nonlinear dynamical networks. Nat Commun. 2016;7: 11323. doi:10.1038/ncomms11323

22. Anderson JR. How can the human mind occur in the physical universe? Oxford ; New York: Oxford University Press; 2007.

23. Staresina BP, Wimber M. A Neural Chronometry of Memory Recall. Trends Cogn Sci. 2019;23: 1071–1085. doi:10.1016/j.tics.2019.09.011

24. Desikan RS, Ségonne F, Fischl B, Quinn BT, Dickerson BC, Blacker D, et al. An automated labeling system for subdividing the human cerebral cortex on MRI scans into gyral based regions of interest. Neuroimage. 2006;31: 968–980. doi:10.1016/j.neuroimage.2006.01.021

25. Cavanagh JF, Frank MJ. Frontal theta as a mechanism for cognitive control. Trends Cogn Sci. 2014;18: 414–421. doi:10.1016/j.tics.2014.04.012

26. Sauseng P, Griesmayr B, Freunberger R, Klimesch W. Control mechanisms in working memory: a possible function of EEG theta oscillations. Neurosci Biobehav Rev. 2010;34: 1015–1022. doi:10.1016/j.neubiorev.2009.12.006

27. Rajan A, Siegel SN, Liu Y, Bengson J, Mangun GR, Ding M. Theta Oscillations Index Frontal Decision-Making and Mediate Reciprocal Frontal–Parietal Interactions in Willed Attention. Cereb Cortex. 2019;29: 2832. doi:10.1093/cercor/bhy149

28. Pellegrino G, Tomasevic L, Herz DM, Larsen KM, Siebner HR. Theta Activity in the Left Dorsal Premotor Cortex During Action Re-Evaluation and Motor Reprogramming. Front Hum Neurosci. 2018;12. doi:10.3389/fnhum.2018.00364

29. Canolty RT, Edwards E, Dalal SS, Soltani M, Nagarajan SS, Kirsch HE, et al. High Gamma Power Is Phase-Locked to Theta Oscillations in Human Neocortex. Science. 2006;313: 1626–1628. doi:10.1126/science.1128115

30. Voloh B, Womelsdorf T. A Role of Phase-Resetting in Coordinating Large Scale Neural Networks During Attention and Goal-Directed Behavior. Front Syst Neurosci. 2016;10. doi:10.3389/fnsys.2016.00018

31. Ketz NA, Jensen O, O'Reilly RC. Thalamic pathways underlying prefrontal cortex-medial temporal lobe oscillatory interactions. Trends Neurosci. 2015;38: 3–12. doi:10.1016/j.tins.2014.09.007

32. Stam CJ, van Straaten ECW. Go with the flow: Use of a directed phase lag index (dPLI) to

characterize patterns of phase relations in a large-scale model of brain dynamics. NeuroImage. 2012;62: 1415–1428. doi:10.1016/j.neuroimage.2012.05.050

33. Reinhart RMG. Working memory revived in older adults by synchronizing rhythmic brain circuits. Nat Neurosci. : 16.

34. Hartwigsen G, Siebner HR. Joint Contribution of Left Dorsal Premotor Cortex and Supramarginal Gyrus to Rapid Action Reprogramming. Brain Stimul. 2015;8: 945–952. doi:10.1016/j.brs.2015.04.011

35. Gallivan JP, Chapman CS, Wolpert DM, Flanagan JR. Decision-making in sensorimotor control. Nat Rev Neurosci. 2018;19: 519–534. doi:10.1038/s41583-018-0045-9

36. Skardal PS, Restrepo JG. Hierarchical synchrony of phase oscillators in modular networks. Phys Rev E. 2012;85: 016208. doi:10.1103/PhysRevE.85.016208

37. Breakspear M, Heitmann S, Daffertshofer A. Generative Models of Cortical Oscillations: Neurobiological Implications of the Kuramoto Model. Front Hum Neurosci. 2010;4. doi:10.3389/fnhum.2010.00190

38. Maistrenko YL, Lysyansky B, Hauptmann C, Burylko O, Tass PA. Multistability in the Kuramoto model with synaptic plasticity. Phys Rev E. 2007;75: 066207. doi:10.1103/PhysRevE.75.066207

39. Deco G, Cabral J, Woolrich MW, Stevner ABA, van Hartevelt TJ, Kringelbach ML. Single or multiple frequency generators in on-going brain activity: A mechanistic whole-brain model of empirical MEG data. NeuroImage. 2017;152: 538–550. doi:10.1016/j.neuroimage.2017.03.023

40. Saalmann YB, Pinsk MA, Wang L, Li X, Kastner S. The Pulvinar Regulates Information Transmission Between Cortical Areas Based on Attention Demands. Science. 2012;337: 753–756. doi:10.1126/science.1223082

41. Sherman SM. The thalamus is more than just a relay. Curr Opin Neurobiol. 2007;17: 417–422. doi:10.1016/j.conb.2007.07.003

42. Ramcharan EJ, Gnadt JW, Sherman SM. Higher-order thalamic relays burst more than first-order relays. Proc Natl Acad Sci USA. 2005;102: 12236–12241. doi:10.1073/pnas.0502843102

43. Kloc M, Maffei A. Target-Specific Properties of Thalamocortical Synapses onto Layer 4 of Mouse Primary Visual Cortex. J Neurosci. 2014;34: 15455–15465. doi:10.1523/JNEUROSCI.2595-14.2014

44. Izzo D, Ruciński M, Biscani F. The Generalized Island Model. Parallel Architectures and Bioinspired Algorithms. 2012; 151–169. doi:10.1007/978-3-642-28789-3_7

45. Behrens TEJ, Johansen-Berg H, Woolrich MW, Smith SM, Wheeler-Kingshott C a. M, Boulby PA, et al. Non-invasive mapping of connections between human thalamus and cortex using diffusion imaging. Nat Neurosci. 2003;6: 750–757. doi:10.1038/nn1075

46. Qin Y, Kawano Y, Portoles O, Cao M. Partial Phase Cohesiveness in Networks of Networks of Kuramoto Oscillators. IEEE Trans Automat Contr. 2021; 1–1. doi:10.1109/TAC.2021.3062005

47. Nicosia V, Valencia M, Chavez M, Díaz-Guilera A, Latora V. Remote Synchronization Reveals Network Symmetries and Functional Modules. Phys Rev Lett. 2013;110: 174102. doi:10.1103/PhysRevLett.110.174102

48. Petkoski S, Spiegler A, Proix T, Aram P, Temprado J-J, Jirsa VK. Heterogeneity of time delays determines synchronization of coupled oscillators. Phys Rev E. 2016;94: 012209. doi:10.1103/PhysRevE.94.012209

49. Vicente R, Gollo LL, Mirasso CR, Fischer I, Pipa G. Dynamical relaying can yield zero time lag neuronal synchrony despite long conduction delays. Proc Natl Acad Sci USA. 2008;105: 17157–17162. doi:10.1073/pnas.0809353105

50. Halgren M, Ulbert I, Bastuji H, Fabó D, Erőss L, Rey M, et al. The generation and propagation of the human alpha rhythm. Proc Natl Acad Sci USA. 2019;116: 23772–23782. doi:10.1073/pnas.1913092116

51. Gramfort A, Luessi M, Larson E, Engemann DA, Strohmeier D, Brodbeck C, et al. MNE software for processing MEG and EEG data. NeuroImage. 2014;86: 446–460. doi:10.1016/j.neuroimage.2013.10.027

52. Fischl B. FreeSurfer. NeuroImage. 2012;62: 774–781. doi:10.1016/j.neuroimage.2012.01.021

53. Oostenveld R, Fries P, Maris E, Schoffelen J-M. FieldTrip: Open Source Software for Advanced Analysis of MEG, EEG, and Invasive Electrophysiological Data. In: Computational Intelligence and Neuroscience [Internet]. Hindawi; 23 Dec 2010 [cited 10 Feb 2021] p. e156869. doi:https://doi.org/10.1155/2011/156869

54. Yu S-Z. Hidden semi-Markov models. Artificial Intelligence. 2010; 29.

55. Ott E, Antonsen TM. Low dimensional behavior of large systems of globally coupled oscillators. Chaos. 2008;18: 037113. doi:10.1063/1.2930766

56. Montbrió E, Pazó D, Roxin A. Macroscopic Description for Networks of Spiking Neurons. Phys Rev X. 2015;5: 021028. doi:10.1103/PhysRevX.5.021028

57. Wildie M, Shanahan M. Metastability and chimera states in modular delay and pulse-coupled oscillator networks. Chaos. 2012;22: 043131. doi:10.1063/1.4766592

58. Cabral J, Luckhoo H, Woolrich M, Joensson M, Mohseni H, Baker A, et al. Exploring mechanisms of spontaneous functional connectivity in MEG: how delayed network interactions lead to structured amplitude envelopes of band-pass filtered oscillations. Neuroimage. 2014;90: 423–435. doi:10.1016/j.neuroimage.2013.11.047

59. Hansen N. The CMA Evolution Strategy: A Comparing Review. : 28.

60. Biscani F, Izzo D. A parallel global multiobjective framework for optimization: pagmo. Journal of Open Source Software. 2020;5: 2338. doi:10.21105/joss.02338

61. Van Essen DC, Ugurbil K, Auerbach E, Barch D, Behrens TEJ, Bucholz R, et al. The Human Connectome Project: a data acquisition perspective. Neuroimage. 2012;62: 2222–2231. doi:10.1016/j.neuroimage.2012.02.018

62. Glasser MF, Sotiropoulos SN, Wilson JA, Coalson TS, Fischl B, Andersson JL, et al. The minimal preprocessing pipelines for the Human Connectome Project. Neuroimage. 2013;80: 105–124. doi:10.1016/j.neuroimage.2013.04.127

63. Sotiropoulos SN, Jbabdi S, Xu J, Andersson JL, Moeller S, Auerbach EJ, et al. Advances in diffusion MRI acquisition and processing in the Human Connectome Project. Neuroimage. 2013;80: 125–143. doi:10.1016/j.neuroimage.2013.05.057

64. Zhang Y, Brady M, Smith S. Segmentation of brain MR images through a hidden Markov random field model and the expectation-maximization algorithm. IEEE Trans Med Imaging. 2001;20: 45–57. doi:10.1109/42.906424

65. Patenaude B, Smith SM, Kennedy DN, Jenkinson M. A Bayesian model of shape and appearance for subcortical brain segmentation. Neuroimage. 2011;56: 907–922. doi:10.1016/j.neuroimage.2011.02.046

66. Tournier J-D, Calamante F, Connelly A. Robust determination of the fibre orientation distribution in diffusion MRI: Non-negativity constrained super-resolved spherical deconvolution. NeuroImage. 2007;35: 1459–1472. doi:10.1016/j.neuroimage.2007.02.016

67. Tournier J-D, Smith R, Raffelt D, Tabbara R, Dhollander T, Pietsch M, et al. MRtrix3: A fast, flexible and open software framework for medical image processing and visualisation. Neuroimage. 2019;202: 116137. doi:10.1016/j.neuroimage.2019.116137

68. Dhollander T, Raffelt D, Connelly A. Unsupervised 3-tissue response function estimation from single-shell or multi-shell diffusion MR data without a co-registered T1 image. 2016.

69. Jeurissen B, Tournier J-D, Dhollander T, Connelly A, Sijbers J. Multi-tissue constrained spherical deconvolution for improved analysis of multi-shell diffusion MRI data. Neuroimage. 2014;103: 411–426. doi:10.1016/j.neuroimage.2014.07.061

70. Raffelt D, Dhollander T, Tournier J-D, Tabbara R, Smith R, Pierre E, et al. Bias Field Correction and Intensity Normalisation for Quantitative Analysis of Apparent Fibre Density. 2017.

71. Tournier J-D, Calamante F, Connelly A. Improved probabilistic streamlines tractography by 2 nd order integration over fibre orientation distributions. 2009 [cited 10 Feb 2021]. Available: /paper/Improved-probabilistic-streamlines-tractography-by-Tournier-Calamante/b4ffcb9ec889a8a68bffc46387a96b78a50ef94a

72. Smith RE, Tournier J-D, Calamante F, Connelly A. Anatomically-constrained tractography: improved diffusion MRI streamlines tractography through effective use of anatomical information. Neuroimage. 2012;62: 1924–1938. doi:10.1016/j.neuroimage.2012.06.005

73. Smith RE, Tournier J-D, Calamante F, Connelly A. SIFT2: Enabling dense quantitative assessment of brain white matter connectivity using streamlines tractography. Neuroimage. 2015;119: 338–351. doi:10.1016/j.neuroimage.2015.06.092

74. Smith RE, Tournier J-D, Calamante F, Connelly A. The effects of SIFT on the reproducibility and biological accuracy of the structural connectome. Neuroimage. 2015;104: 253–265. doi:10.1016/j.neuroimage.2014.10.004

75. Smith R, Raffelt D, Tournier J-D, Connelly A. Quantitative streamlines tractography: methods and inter-subject normalisation. OSF Preprints; 2020. doi:10.31219/osf.io/c67kn

76. Roberts JA, Perry A, Roberts G, Mitchell PB, Breakspear M. Consistency-based thresholding of the human connectome. NeuroImage. 2017;145: 118–129. doi:10.1016/j.neuroimage.2016.09.053

644

645

646